



# Seismic Control of Base-Isolated Liquid Storage Tanks Subjected to Bi-directional Strong Ground Motions

Sourabh Vern<sup>1</sup> · M. K. Shrimali<sup>1</sup> · S. D. Bharti<sup>1</sup> · T. K. Datta<sup>2</sup> · Ehsan Noroozinejad Farsangi<sup>3</sup>

Received: 6 May 2021 / Accepted: 24 August 2021 / Published online: 8 September 2021  
© King Fahd University of Petroleum & Minerals 2021

## Abstract

Damage of liquid storage tanks (LSTs) due to earthquakes has increased the base isolation systems' demand. As base isolation is a proven control system for mitigating the damages in typical load-bearing structures, its implementation in LSTs is undoubtedly of interest. In the current study, the seismic performance of the base-isolated 3D model of concrete LSTs is investigated under two-component earthquakes as not much literature is available on the subject. The ABAQUS software is used for non-linear analyses of the base-isolated LST in which liquid and isolators are modeled by the arbitrary Lagrangian–Eulerian and connector elements. For the numerical study, two concrete LSTs of the square and rectangular plans are considered with five lead rubber bearing isolators. The change in response quantities of interest is evaluated under parametric variations, including the type of earthquake, peak ground acceleration, the angle of incidence of the earthquake, and the effective period of the isolator. The response quantities of interest considered are shear forces, overturning moments, top board displacements, hydrodynamic pressure, sloshing height, and Von-Mises stress. The results of the numerical investigation show that the efficacy of base-isolated 3D LST should be assessed at least under a two-component earthquake. Further, the study shows that base isolation is highly effective in controlling seismic stresses developed in LST under two-component earthquakes.

**Keywords** Liquid storage tank · LRB · Bi-directional ground motion · Sloshing height · FEM

## 1 Introduction

Concrete ground supporting LSTs are among the critical and widespread civil structures used for storage and supply purposes in oil refineries, chemical industries, nuclear power plants, drainage facilities, sewage treatment plants, and railway industries. Failure of these structures results in severe disaster to the nearby surrounding environment, and their repercussions can last up to a long time. To protect from such shortcomings, control mechanisms are required to ensure LSTs' fail-safe operations under the design and extreme level of earthquakes [1–6].

To successfully implement any control mechanism in the LST, its seismic behavior needs more understanding, as it may behave differently from a regular load-bearing structure. The responses of LSTs are divided into two major parts, namely impulsive and convective. The impulsive response helps determine the shear force, overturning moment, hydrodynamic pressure, and Von-Mises stress. On the contrary, the contribution of the convective response is most notable for the sloshing height. Thus, to mitigate the seismic forces induced in the LST, both impulsive and convective responses

---

✉ Ehsan Noroozinejad Farsangi  
noroozinejad@kgut.ac.ir

Sourabh Vern  
sourabh.vern@gmail.com

M. K. Shrimali  
shrimalimk@gmail.com

S. D. Bharti  
sdbharti@mnit.ac.in

T. K. Datta  
tushar\_k\_datta@yahoo.com

<sup>1</sup> National Center for Disaster Mitigation and Management, Malaviya National Institute of Technology, Jaipur, Jaipur 302017, India

<sup>2</sup> Indian Institute of Technology Delhi, New Delhi 110016, India

<sup>3</sup> Faculty of Civil and Surveying Engineering, Graduate University of Advanced Technology, Kerman, Iran



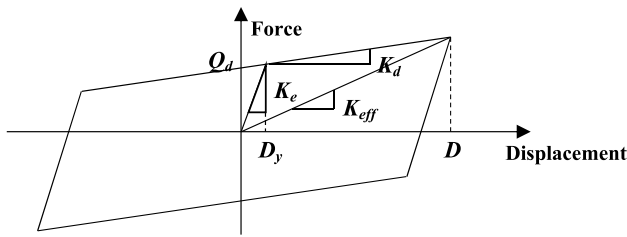


Fig. 1 Bilinear behavior of the LRB Isolator

must be controlled to such an extent that they can operate even after a significant seismic event [1, 4, 7, 8].

The most commonly accepted analytical model of LSTs was given by Housner [9, 10]. Extending Housner's study, several researchers provided the behavioral understanding of the LSTs for the harmonic and irregular support base excitations [11–14]. The analytical solutions were further extended in numerical methods and closed-form solutions [13, 15, 16]. With the significant numerical complexities, and the inability of the above-mentioned numerical approaches for nonlinear behavior of fluid sloshing, the finite element method (FEM), becomes famous for the seismic analysis of LSTs [5, 17–21]. With the availability of the standard finite element software, the study of LSTs under earthquake excitations becomes less computationally demanding [22–27].

Many researchers have extensively studied the seismic response control by base isolation in many load-bearing structures [28–32]. Similarly, base isolation implementation in LSTs also attracted the attention of many researchers [33, 34]. Jing et al. [35] studied the effect of a sliding base-isolated system for a concrete rectangular liquid tank at various liquid heights. The results concluded that by applying the isolation measures, the horizontal displacement of the tank wall was controlled.

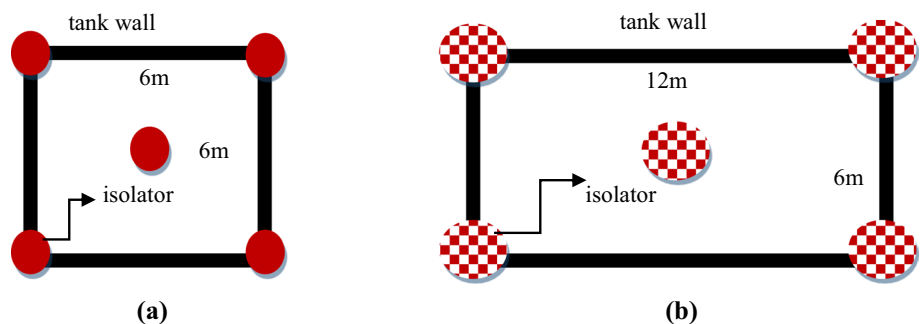
The analysis of the isolated LSTs under seismic excitations for multicomponent ground motion is relatively new. More recently, Hashemi and Aghashiri [36] examined seismic responses of a pool-sized rectangular base-isolated LST for the bi-directional earthquake ground motions. The lead rubber bearing (LRB) and friction pendulum system (FPS) isolator systems were taken for the study. It was concluded that the shear force, wall deflection, and hydrodynamic pressure get reduced due to seismic isolation. Jing et al. [35] described the importance of considering the bi-directional earthquakes in place of unidirectional earthquakes to analyze LSTs with friction isolation. It was concluded that sliding isolation devices can significantly decrease the risk of failures. Rawat et al. [37] studied the behavior of the cylindrical base-isolated steel LSTs under the bi-directional earthquake excitation by the FEM in the ABAQUS. The FPS and LRB isolation systems were modeled with the help of the connector elements.

Although the seismic response behavior analysis of both steel and concrete LSTs has been investigated in the past for a broad spectrum of influencing variables, the same for the base-isolated concrete LSTs is relatively more minor [25, 36, 38, 39]. In particular, the effectiveness of base isolation in improving the seismic behavior of 3D concrete LSTs under bi-directional earthquake excitation has not been investigated through an exhaustive parametric study. In this paper, a comprehensive study of two 3D concrete base-isolated LSTs is conducted to determine the effectiveness of the base isolation technique in LSTs under a set of critical parametric variations. This includes the effectiveness of base isolation in terms of (i) the type of earthquake; (ii) the reduction in different response quantities of interest; (iii) the spillage of liquid; (iv) the characteristics of isolators; and (v) the earthquake incidence angle.

Table 1 Properties of 3D LSTs and fluid

Concrete	Liquid (water)
Modulus of elasticity, $E_c = 24.86$ GPa	Density, $\rho_w = 983.204$ kg/m <sup>3</sup>
Density, $\rho_c = 2450$ kg/m <sup>3</sup>	Equation of state: $c_0 = 1450, s = 0, \gamma_0 = 0$
Poisson's ratio, $\nu = 0.17$	Dynamic viscosity = $0.001$ N s/m <sup>2</sup>

Fig. 2 Arrangements of base isolators plan view of the LST with isolators a square tank b rectangular tank



## 2 Modeling Approach

The concrete LST is designed for the combination of gravity and seismic loads. The base of the LST is supported by the base isolators, which rest on the hardened floor. The laminated rubber bearing lacks high energy dissipation properties, which are not helpful when the intensity of

the earthquakes is high. Thus, a more effective isolation system has opted for the lead core rubber bearing (LRB). Due to its central lead core, the additional energy dissipation property is fed into the isolation system, which results in the augmented size of the hysteresis loop of the isolator system. The nonlinear behavior of the LRB isolation system (LRB) has been idealized by various models [30, 40–42]. Among them, Wen's model [30] is widely used

**Table 2** Properties of isolators designed for different vibration periods

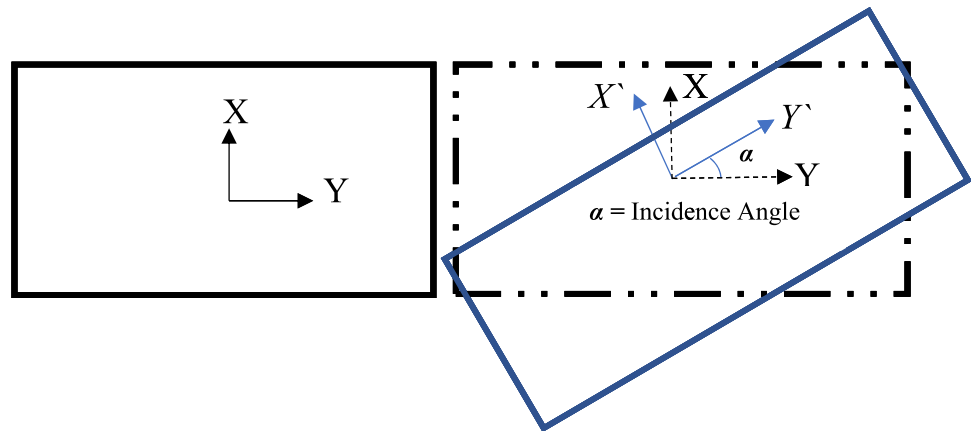
Isolation period, $T_b$ (s)	Effective stiffness, $K_{eff}$ (kN/m)		Elastic stiffness, $K_e$ (kN/m)		Post-yield stiffness ratio, $\gamma = K_d/K_e$		Characteristic strength $Q_d$ (kN)	
	Square LST	Rectangular LST	Square LST	Rectangular LST	Square LST	Rectangular LST	Square LST	Rectangular LST
0.85	2242	4385	17,690	33,521	0.09	0.09	29	61
1.00	1620	3170	12,781	24,219	0.09	0.09	25	49
1.50	720	1405	5680	10,764	0.09	0.09	18	41
2.00	405	790	3195	6055	0.09	0.09	16	34
2.25	320	625	2525	4784	0.09	0.09	14	25
2.50	260	506	1980	3875	0.09	0.09	12	19
3.00	180	352	1420	2691	0.09	0.09	10	17

**Table 3** Details of earthquake ground motions

S. no	Year	Earthquake	Station	Magnitude	PGA (g)	$R_{jb}$ (km)	Mechanism
<i>Far-field records</i>							
1	1995	Kern County	Taft Lincoln school	7.3	0.18	38.42	Reverse
2	1992	Landers	Cool water	7.3	0.41	19.74	Strike-slip
3	1978	Tabas	Ferdows	7.4	0.11	89.76	Reverse
4	1995	San Fernando	LA Hollywood store	6.6	0.22	22.77	Reverse
5	1987	Superstition hill	Poe road	6.5	0.47	17.03	Strike-slip
6	1989	Loma Prieta	Sunol-forest fire St	6.9	0.08	47.41	Strike-slip
7	1994	Northridge-01	Downy-Co Maint	6.6	0.15	43.20	Reverse
<i>Near-field records (Fling step effect)</i>							
1	1999	Chi Chi	TCU 052	7.6	0.44	1.8	Reverse oblique
2	1999	Chi Chi	TCU 068	7.6	0.36	3.0	Reverse oblique
3	1999	Kocaeli	Sakarya	7.4	0.41	3.2	Strike-slip
4	1999	Chi Chi	TCU 065	7.6	0.76	2.5	Reverse oblique
5	1999	Kocaeli	Yarimaca	7.5	0.23	1.3	Strike-slip
6	1999	Chi Chi	TCU 076	7.6	0.34	2.8	Reverse oblique
7	1999	Chi Chi	TCU 089	7.6	0.35	0.0	Reverse oblique
<i>Near-field records (Low directivity effect)</i>							
1	1989	Loma Prieta	Gilroy Array#3	6.9	0.36	12.23	Reverse oblique
2	1995	Kobe	Takarazuka	6.9	0.69	0.0	Strike-slip
3	1989	Loma Perieta	Saratogo Aloha Ave	6.9	0.32	7.58	Reverse oblique
4	2004	Parkfield	EADES	6.0	0.39	6.0	Strike-slip
5	2004	Parkfield	Chalome 1E station	6.0	0.44	1.66	Strike-slip
6	1994	Northridge-01	Jensen Filter plant	6.6	0.41	0.0	Reverse
7	1994	Northridge-01	LA Dam	6.6	0.43	0.0	Reverse

$R_{jb}$  (Joyner–Boore distance to rupture plane)

**Fig. 3** Variation of the angle of incidence in LSTs



for the LRB isolator. The advantage of Wen's model is that many experimental tests verify its idealization of the bilinear hysteretic model. Wen's bilinear hysteretic model is adopted in the study and is shown in Fig. 1.

For the circular base isolator, it can be assumed that the hysteretic behavior of the isolator is homogenous in all directions. As a consequence, the bilinear hysteretic properties of the isolator remain the same under the bi-directional earthquakes, independent of the directional movement of the isolator, unlike the square isolator. The bilinear curve consists of three salient parameters, namely (i) yield strength  $F_y$ ; (ii) characteristic strength  $Q_d$ ; and (iii) post-yield stiffness ratio ( $K_d/K_e$  or  $K_2/K_1$ ). The characteristic strength is the intercept of force at the displacement value of zero. The characteristic strength of the LRB isolator is determined by the yield strength of lead in shear,  $f_{py}$  for a given area of  $A_p$  as presented by Eq. (1) [32]

$$Q_d = f_{py} \times A_p \quad (1)$$

The relationship between the post-yield stiffness,  $K_d$ , and the effective stiffness,  $K_{eff}$ , at the specified design displacement  $D$  and  $Q_d$  is given by Eq. (2)

$$K_d = K_{eff} - \frac{Q_d}{D} \quad (2)$$

For estimating the effective damping of the LRB,  $\beta_{eff}$  for a specified yield displacement  $D_y$  is given by Eq. (3)

$$\beta_{eff} = \frac{2Q_d}{\pi D^2 K_{eff}} (D - D_y) \quad (3)$$

The time history analysis of the concrete LSTs with the LRB isolators is computationally intensive and involves many complexities. The LST is modeled by an eight noded linear brick element (C3D8R) in the current study, with hourglass control and a reduced integration scheme available in the ABAQUS. In contrast, the isolators are modeled by two-noded connector elements. The same brick element model

the fluid as the tank to comprehend and simulate the sloshing in the LST. A suitable mesh control technique is required as the fluid simulation involves the mesh's distortion to a huge factor. The finite element analysis offers a couple of analysis approaches, commonly known as the Lagrangian and Eulerian approaches. In the Eulerian analysis, the material can pass through the fixed mesh boundaries; thus, avoiding any distortion of the element. In Lagrangian analysis, the material remains in closed boundaries of the elements, not allowing high distortion.

The arbitrary Lagrangian–Eulerian (ALE) approach is utilized in the current fluid–structure interaction simulation (FSI) to avoid high distortion in the finite elements. Using the ALE to control the distortion in the analysis, the flow of the material and movement induced in the mesh is maintained, resulting in the lower distortion in the mesh. This lower distortion of the mesh provides continuity in the analysis. The ALE formulation employed by the ABAQUS for the current study uses the second-order advection and element center projection momentum advection which require fewer operations [43–45].

The dynamic explicit operator is used for the analysis to capture the liquid sloshing and nonlinear behavior of the isolation system. This operator allows the large deformation theory in the simulation under which elements' large rotations and deformations are possible.

### 3 Numerical Examples

To investigate the control of the seismic response of LSTs, two LSTs are considered for the study, one is a square LST of the dimension  $6 \text{ m} \times 6 \text{ m} \times 4.8 \text{ m}$ , and the other is a rectangular LST of the dimension  $12 \text{ m} \times 6 \text{ m} \times 4.8 \text{ m}$  with a wall thickness of  $0.3 \text{ m}$  in both the LSTs. These sizes are primarily constructed in various chemical and nuclear industries for storage purposes [35, 46–48]. The different material



**Fig. 4** Finite element mesh and connector elements of the LSTs

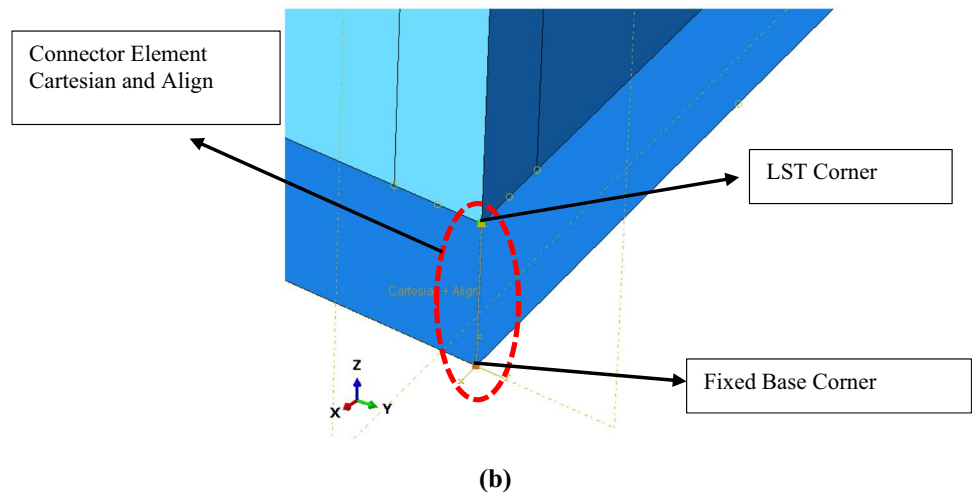
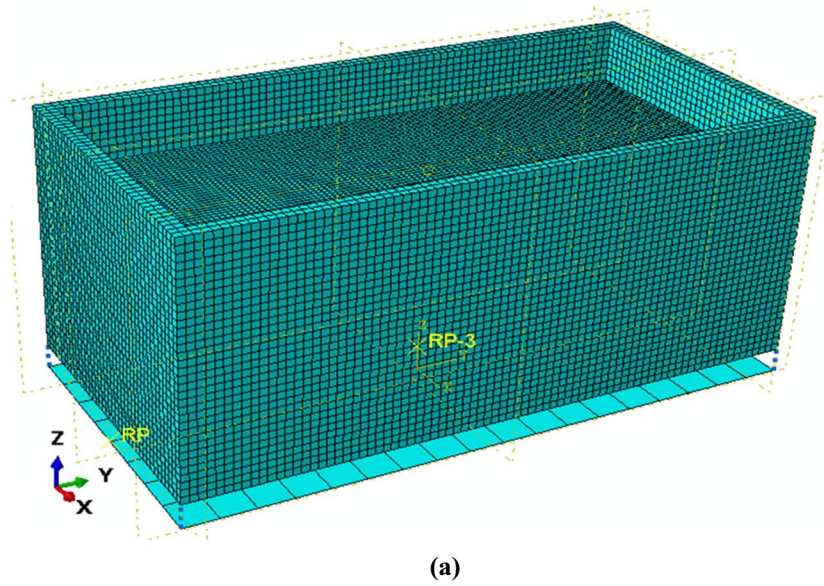


**Table 4** Results of mesh refinement study

Mesh	No. of elements	Displacement of the tank wall	Stress in LST (MPa)	Relative CPU time (s)
Coarse	3684	5.80E-04	1.11	5.5
Normal	12,928	6.25E-04	1.19	20
Fine	20,744	6.40E-04	1.21	80
Very fine	43,632	6.45E-04	1.22	110

properties of the LST and liquid are shown in Table 1 [23, 49].

The height of the liquid in both LST is taken as 3.6 m. Thus, the tanks' *H/L* ratio (in which *H* is the height of the water, and *L* is the larger of the two plan dimensions) is 0.6 and 0.3, respectively. Five LRBs are used for the isolation

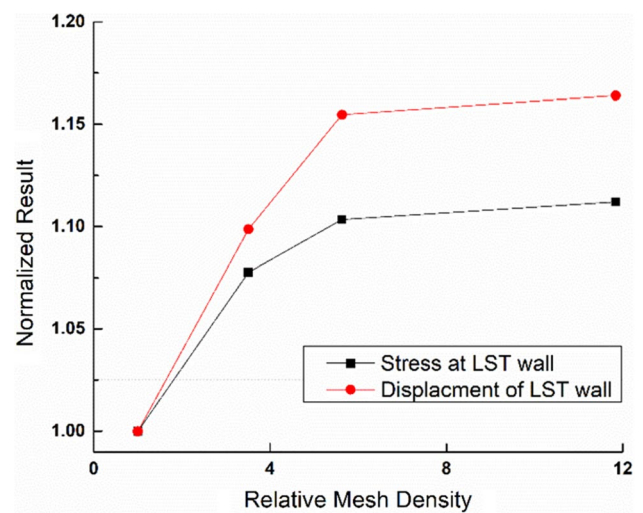
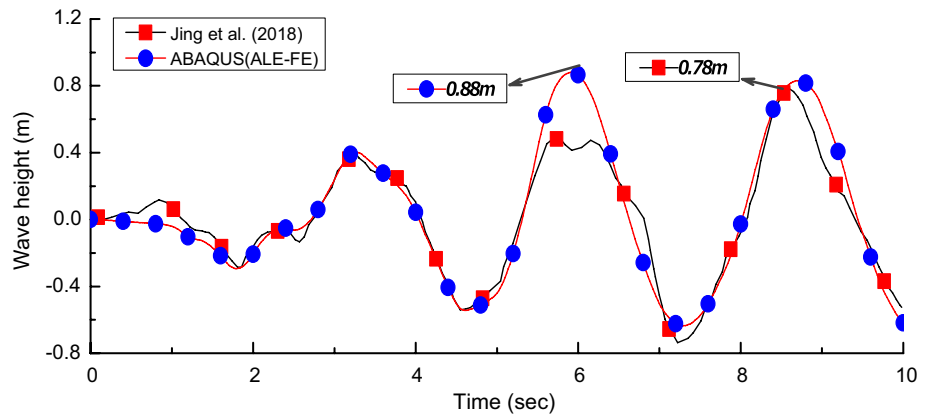


**Fig. 5** Convergence of results in mesh refinement study



**Fig. 6** Validation of base-isolated LST under bi-directional ground motion



of the tank, as shown in Fig. 2. Four isolators are placed at four corners and one at the center bottom of the tank. The LRB isolators are fixed to the rigid floor such that there is no uplifting of the base. The properties of the isolators are shown in Table 2.

Three different types of earthquakes are used to analyze the LST: far-field, near-field with directivity effect, and near-field with the fling step effect. For every kind of earthquake, seven different time history records are taken as recommended by Reyes and Kalkan [50]. The details of the time histories of the earthquake are shown in Table 3. The earthquakes are scaled to three peak ground accelerations (PGAs), namely 0.2 g, 0.4 g, and 0.6 g, which denotes the event's severity. Both horizontal components of the earthquakes are used in the study for bi-directional excitation, as shown in Fig. 3. The ratio between the horizontal components is taken as 1:0.67.

The isolators are modeled in ABAQUS using connector elements. The connector elements require inputs such as elasticity, damping, and bilinear behavior, in which the half-cycle hardening property is selected. The connector elements taken in the analysis are Cartesian and align. The bottom nodes of connector elements are joined to the rigid surface and top nodes to the bottom of four corners and one

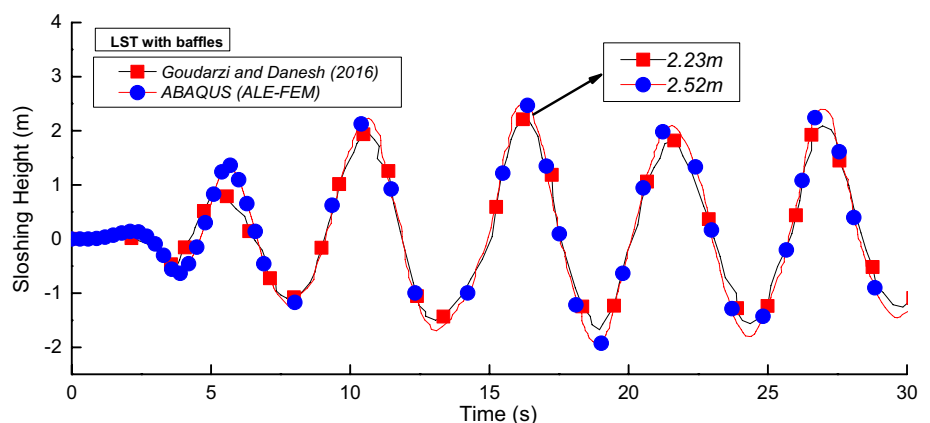
in the LST center. The isolator is provided with high vertical stiffness, which has a rigid effect and avoids LSTs' rocking. The earthquake incidence angle is varied with respect to the X-direction, as shown in Fig. 3. The detailed meshed assembly of the LST with the isolators is demonstrated in Fig. 4.

Unlike the base-isolated buildings, no fixed guidelines are available for obtaining the effective vibration period of isolators in LSTs. Consequently, as shown in Table 2, seven effective isolation periods are considered in the study to get the optimum reduction in responses. To achieve the same isolation period for the two tanks, the effective stiffnesses of the isolators for the square and rectangular tanks are adjusted. The properties of the isolator for each isolation period are shown in Table 2.

## 4 Results and Discussion

The effectiveness of base isolation is investigated for several parameters: the effective time period of the isolator, type of the earthquake, PGA, and the earthquake incidence angle. To describe the effect of the angle of incidence of earthquakes in the base-isolated LSTs, the optimum time period of the isolation system is used. The mean reductions of the four response

**Fig. 7** Validation of nonlinear behavior of the liquid inside the LST under earthquake excitation



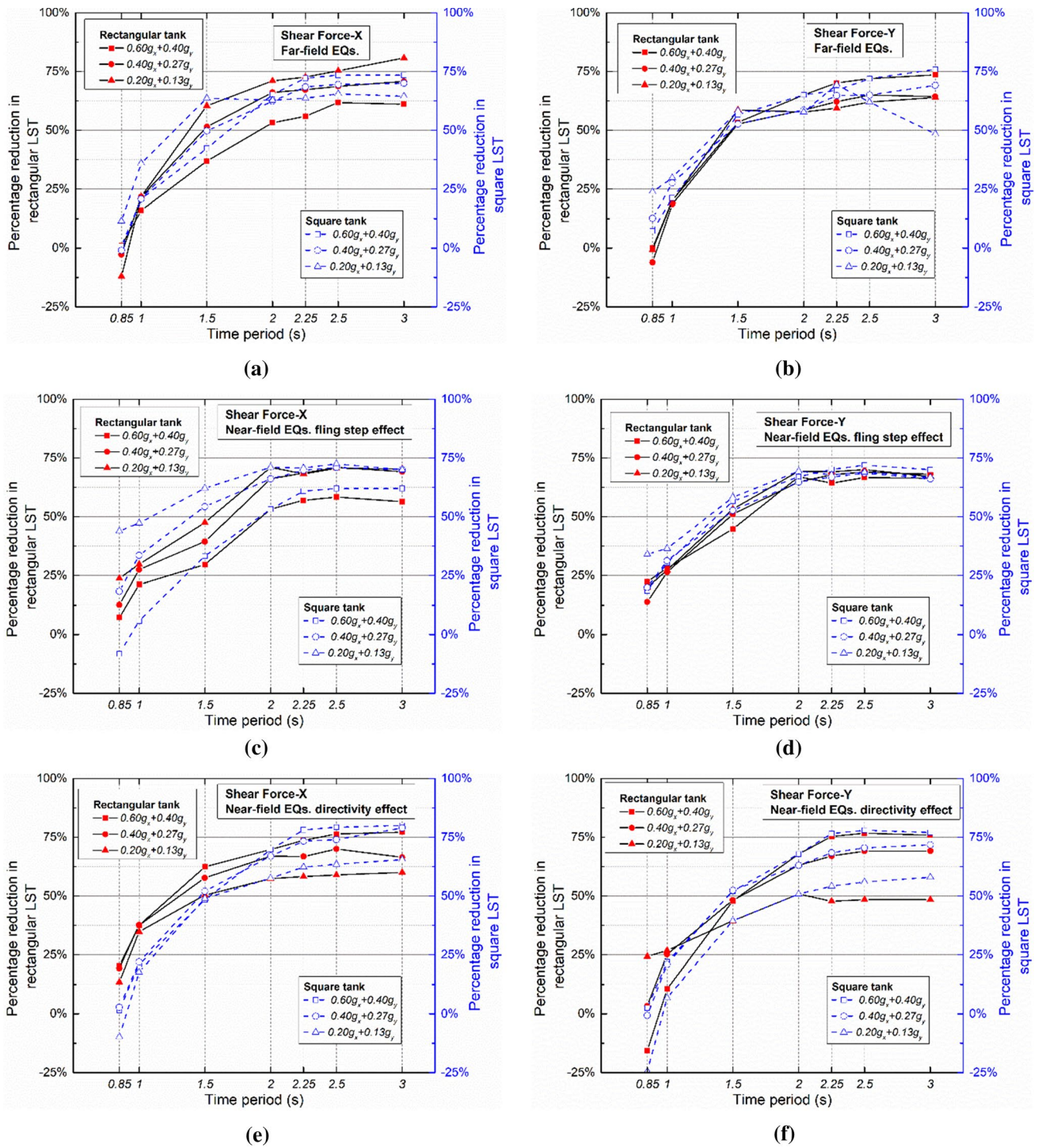


**Fig. 8** Variation of the percentage reduction in shear forces with the time period of the LRB isolators for different LSTs; **a, b** far-field earthquakes, **c, d** near-field earthquakes with fling step effect, **e, f** near-field earthquakes with directivity effect

quantities are evaluated, which are shear forces (X and Y), overturning moments (X and Y), top board displacements (TBDs) (X and Y), hydrodynamic pressure, and Von-Mises stress to evaluate the effectiveness of the base isolation. The mean amplification in sloshing height is examined to arrive at

the optimum time period of the base isolator in the LSTs. The shear forces, overturning moments are recorded at the rigid plate base, whereas top board displacement is calculated at the LST walls. The maximum hydrodynamic pressure acting on the tank walls and corners is noted by considering maximum

**Table 5** Maximum percentage reduction in the shear force in X-direction for different earthquakes

Response	PGA	$T_b$	Type of earthquake					
			Far-field Eqs		Near-field Eqs. with fling step effect		Near-field Eqs. with directivity effect	
			Square LST (%)	Rectan-gular LST (%)	Square LST (%)	Rectan-gular LST (%)	Square LST (%)	Rectan-gular LST (%)
Shear force-X	$0.6g_x + 0.4g_y$	1.5	42	37	33	30	48	62
		2.0	65	53	53	53	70	70
		2.5	74	62	62	58	79	76
	$0.4g_x + 0.27g_y$	1.5	50	51	54	39	52	58
		2.0	62	66	66	66	67	67
		2.5	70	69	71	71	74	70
	$0.2g_x + 0.13g_y$	1.5	64	60	62	48	49	50
		2.0	63	71	71	71	58	57
		2.5	66	75	73	71	64	59

$g_x$  (horizontal component of the earthquake in X-direction),  $g_y$  (horizontal component of the earthquake in Y-direction)

**Table 6** Maximum percentage reduction in the shear force in Y-direction for different earthquakes

Response	PGA	$T_b$	Type of earthquake					
			Far-field Eqs		Near-field Eqs. with fling step effect		Near-field Eqs. with directivity effect	
			Square LST (%)	Rectan-gular LST (%)	Square LST (%)	Rectan-gular LST (%)	Square LST (%)	Rectan-gular LST (%)
Shear force-Y	$0.6g_x + 0.4g_y$	1.5	53	53	57	45	52	48
		2.0	65	65	67	67	68	68
		2.5	72	72	72	67	78	77
	$0.4g_x + 0.27g_y$	1.5	53	53	53	51	52	48
		2.0	59	59	65	65	63	63
		2.5	65	65	69	69	71	69
	$0.2g_x + 0.13g_y$	1.5	59	59	58	53	40	39
		2.0	58	58	69	69	51	51
		2.5	62	62	69	70	56	48

$g_x$  (horizontal component of the earthquake in X-direction),  $g_y$  (horizontal component of the earthquake in Y-direction)

pressure in all directions to reduce the hydrodynamic pressure. Because of this reason, the direction of the maximum decrease in hydrodynamic pressure is also not mentioned. A spatial envelope of the liquid height for the base-isolated and uncontrolled LSTs is compared to determine the reduction in sloshing height. To assess the accuracy of results mesh convergence study is done. To study the influence of the mesh density of the LST, two different response quantities, namely top board displacement and stress in the wall, are considered here. The comparison between four different mesh densities is shown in Table 4. It can be seen from Fig. 5 that coarse mesh yields less accurate values of the displacements and stress in the LST;

however, the normal, fine, and very fine meshes yield results of a similar order. As the displacement and stress value is converged, the normal mesh is opted for further study. For the better accuracy of results, a mesh convergence study was carried out. Based on that, an element size of  $0.15 \text{ m} \times 0.15 \text{ m} \times 0.15 \text{ m}$  for LST and  $0.075 \text{ m} \times 0.075 \text{ m} \times 0.075 \text{ m}$  for liquid is selected.

#### 4.1 Validation of Current FE Model

Two different validation studies are conducted to validate the accuracy of responses obtained by the current ALE-FE approach. In the first one, the sloshing height of the



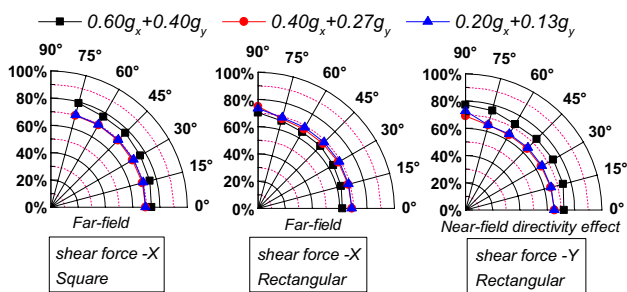


**Fig. 9** Variation of the percentage reduction in shear forces with the angle of incidence for square and rectangular LSTs

base-isolated LST obtained by Jing et al. [35] is compared with the ALE-FE approach. In the second one, the nonlinear behavior of the liquid is studied. To further check the accuracy of the current ALE-FE approach, results of the sloshing response of LST with internal hindrance are used by Goudarzi and Danesh [51].

**4.1.1 Validation of Base-Isolated LST Under Bi-directional Ground Motion**

Figure 6 shows the sloshing height response obtained by Jing et al. [35] and the current ALE-FE approach with connector elements. The LST is a square plan with dimensions 6 m × 6 m × 4.8 m with a liquid height of 3.6 m and a wall thickness of 0.3 m. It can be seen from Fig. 6 that the time histories of the sloshing height obtained by the current ALE-FE approach are relatively the same with a percentage of error of 11%. Therefore, it can be established that the types of elements for LST, liquid, and isolator are correct.

**4.1.2 Validation of Nonlinear Behavior of the Liquid Inside the LST Under Earthquake Excitation**

To validate the accuracy of the current ALE-FE approach in accurately capturing the nonlinear nature of the liquid, the sloshing height response obtained by Goudarzi and Danesh [51] is compared. In the study, a computational fluid dynamics (CFD) code in the commercial FE software ANSYS was used in which liquid was modeled by Eulerian-Eulerian homogenous model. According to Goudarzi and Danesh [51], liquid sloshing's nonlinear behavior and interaction with LST walls were duly considered. The comparison between the sloshing height obtained by the ALE-FE approach and Goudarzi and Danesh [51] is shown in Fig. 7. It can be seen from the results that both approaches are perfectly capable of capturing the nonlinearity of liquid quite effectively with a 12% of error.

**4.2 Shear Force**

Figure 8 shows the variations of the mean percentage reduction in the shear forces (X and Y) with the isolator's effective time period ( $T_b$ ) in both X- and Y-directions for square and rectangular LSTs. It is seen from the figures that the reduction in the shear forces generally increases with an increase in  $T_b$ . However, the increase in the mean percentage reduction of shear forces is not very significant after the value of  $T_b = 2.0$  s. In fact, beyond a value of  $T_b = 2.5$  s, the curve showing the variation of the mean percentage reduction becomes almost flat. The maximum reduction in the shear forces is of the order of 75% for both tanks. Thus, the optimum time period of isolation from considering the maximum reduction in base shear is 2.5 s.

The pattern variation of the mean percentage reduction of the shear forces with  $T_b$  is different for different types of earthquakes up to  $T_b = 1.5$  s; after that, the variation pattern is nearly the same for all types of earthquakes. Tables 5 and 6 show the mean percentage reduction of shear forces in both tanks for three specific values of  $T_b = 1.5$  s, 2.0 s, and 2.5 s for different types of earthquakes.

It can be seen from Tables 5 and 6 that all types of earthquakes provide a relatively similar reduction in the shear forces, except at lower PGA levels for the case of the rectangular LST, where the reduction under near-field earthquakes has been marginally higher. The absence of any consistent pattern in the reduction variation might be because the reduction is calculated as the mean reduction in the response for the five different earthquake records having varying energy contents. The reduction in response depends on the energy density bandwidth, frequency contents of the earthquake, and natural frequency of the structure. Further, the relationship between the PGA and mean percentage reduction in responses does not show any consistent pattern, and it varies with the type of earthquake. The reduction of shear forces in the LSTs varies with PGA change, but it does not follow any definite trend. This happens because the reduction in shear forces is a complicated event comprising different earthquake frequency contents and nonlinearity produced because of complex fluid–structure interaction. As a result, no apparent pattern of results emerges when the change in responses is averaged over those obtained from an array of earthquake datasets corresponding to a particular type of earthquake.

A few sample plots of the variation of mean percentage reduction in the shear forces with the angle of incidence of the earthquake are shown in Fig. 9. It is clear from the figures that the percentage of reduction in the shear forces remains nearly the same for all angles of incidence, from 15 to 75 degrees.

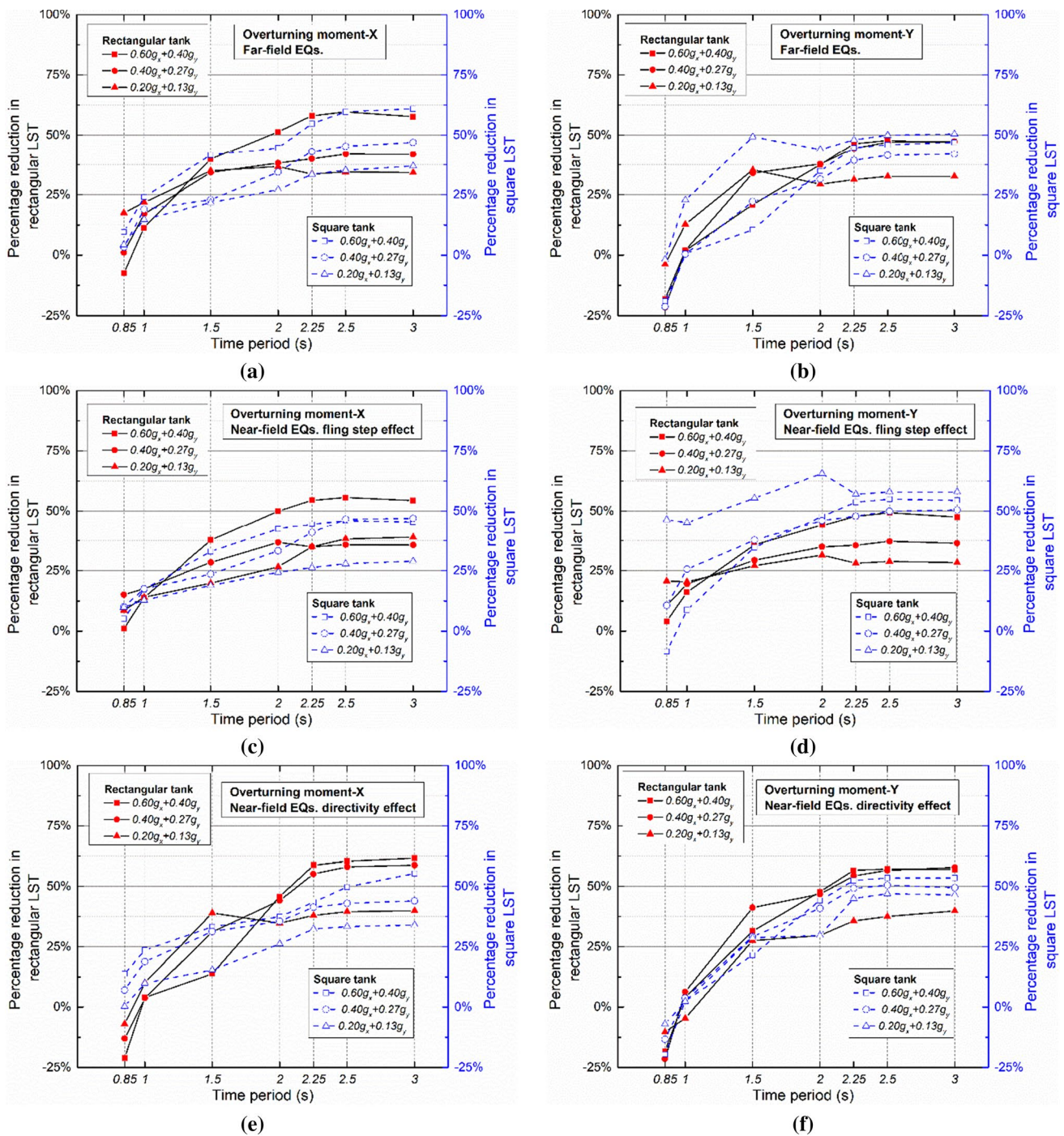


Fig. 10 Variation of the percentage reduction in overturning moment with the time period of the LRB isolators for different LSTs; a, b far-field earthquakes, c, d near-field earthquakes with fling step effect, e, f near-field earthquakes with directivity effect

### 4.3 Overturning Moment

Figure 10 shows the variation of the mean percentage reduction of the overturning moments (in X- and Y-directions) with the isolator's effective time period ( $T_b$ ) for both  $H/L$  ratios. The figures show that the reduction in the overturning moments generally increases with the increase

in  $T_b$  increase for most cases, up to a value of  $T_b = 2.0$  s. After that, the rate of change of the reduction in overturning moments becomes almost stationary. The maximum percentage of reduction in the overturning moments is of the order of 50–60%.

Like the shear forces, the pattern in the variation of the mean percentage reduction of the overturning moments

**Table 7** Maximum percentage reduction in the overturning moment in X-direction for different earthquakes

Response	PGA	$T_b$	Type of earthquake					
			Far-field Eqs		Near-field Eqs. with fling step effect		Near-field Eqs. with directivity effect	
			Square LST (%)	Rectangular LST (%)	Square LST (%)	Rectangular LST (%)	Square LST (%)	Rectangular LST (%)
Overturning moment-X	$0.6g_x + 0.4g_y$	1.5	30	40	46	38	28	14
		2.0	38	51	51	50	42	46
		2.5	47	60	56	56	51	60
	$0.4g_x + 0.27g_y$	1.5	33	34	41	33	32	31
		2.0	29	38	47	42	37	44
		2.5	35	42	50	46	45	58
	$0.2g_x + 0.13g_y$	1.5	49	35	53	28	24	39
		2.0	38	37	61	37	25	35
		2.5	41	35	58	36	32	40

$g_x$  (horizontal component of the earthquake in X-direction),  $g_y$  (horizontal component of the earthquake in Y-direction)

**Table 8** Maximum percentage reduction in the overturning moment in Y-direction for different earthquakes

Response	PGA	$T_b$	Type of earthquake					
			Far-field Eqs		Near-field Eqs. with fling step effect		Near-field Eqs. with directivity effect	
			square LST (%)	rectangular LST (%)	square LST (%)	rectangular LST (%)	square LST (%)	rectangular LST (%)
Overturning moment-Y	$0.6g_x + 0.4g_y$	1.5	10	21	35	36	22	31
		2.0	35	38	48	44	44	48
		2.5	46	48	55	49	54	57
	$0.4g_x + 0.27g_y$	1.5	22	34	38	29	29	41
		2.0	32	38	46	35	41	47
		2.5	42	47	50	37	51	57
	$0.2g_x + 0.13g_y$	1.5	49	35	55	27	29	28
		2.0	44	29	66	32	30	30
		2.5	50	33	58	29	47	38

$g_x$  (horizontal component of the earthquake in X-direction),  $g_y$  (horizontal component of the earthquake in Y-direction)

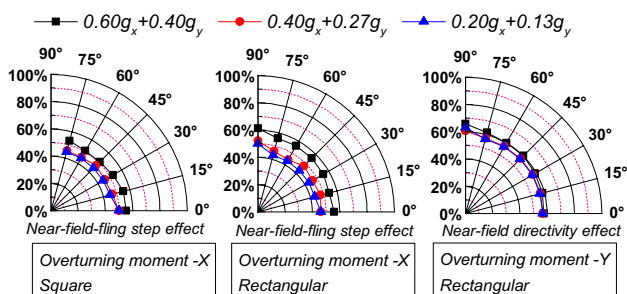


**Fig. 11** Variation of the percentage reduction in overturning moments with the angle of incidence for square and rectangular LSTs

with the  $T_b$  is different for different earthquakes up to  $T_b = 1.5$  s; after that, the pattern of variation does not change significantly.

Tables 7 and 8 show the mean percentage reduction of the overturning moments for the three specific time period values (1.5 s, 2 s, and 2.5 s) for different earthquakes. It is seen from the tables that except for the far-field earthquakes, the near-field earthquakes provide a nearly comparable decrease in the overturning moments; the near-field with directivity effect shows, in general, more percentage reduction in the



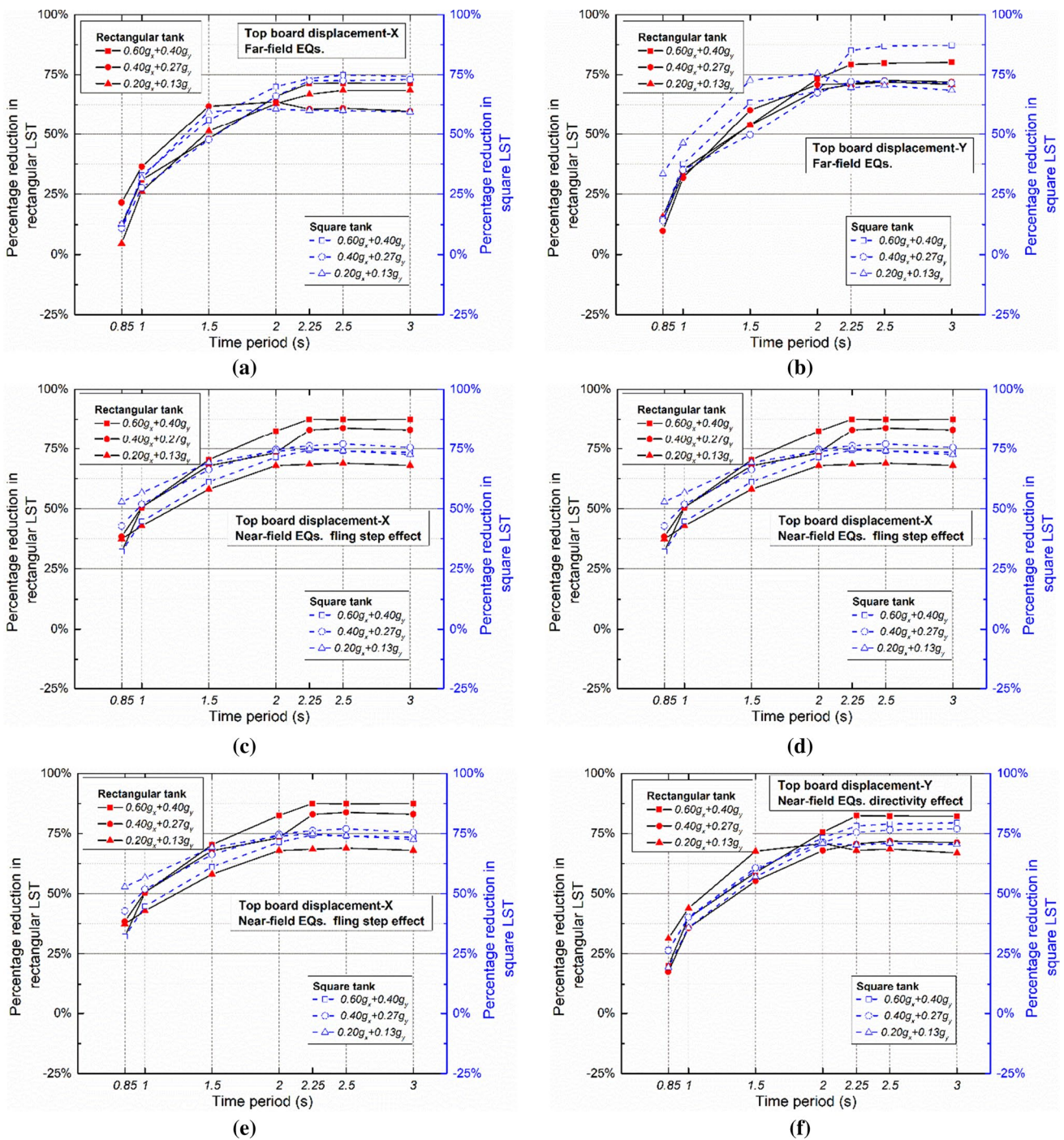


**Fig. 12** Variation of the percentage reduction in top board displacement with the time period of the LRB isolators for different LSTs; **a, b** far-field earthquakes, **c, d** near-field earthquakes with fling step effect, **e, f** near-field earthquakes with directivity effect

overturning moments. The far-field earthquakes provide a minor reduction of the overturning moments.

Like the shear forces, the variation of the mean percentage reduction in the overturning moments with different

PGAs does not show any consistent pattern. As for the variation of reduction in overturning moment with the angle of incidence, it is seen that the percentage reduction is not sensitive to the variation of the angle of incidence of earthquake



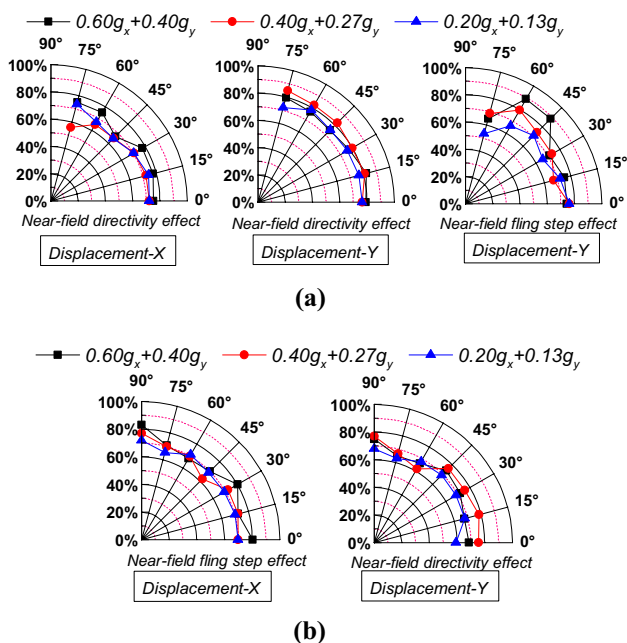


Fig. 13 Variation of the percentage reduction in TBDs with the angle of incidence for a square LST b rectangular LSTs

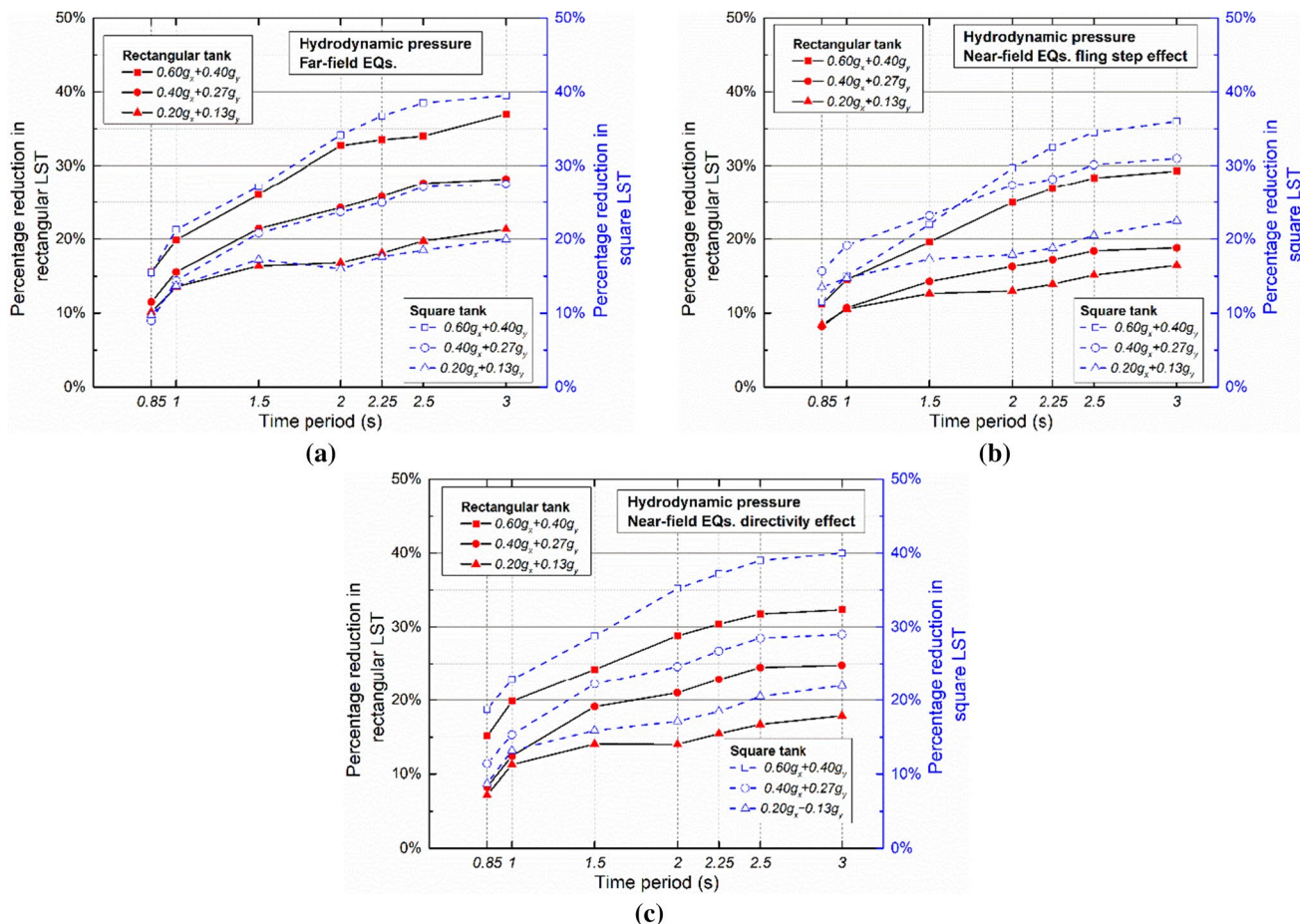


Fig. 14 Variation of the percentage reduction in hydrodynamic pressure with the time period of the LRB isolators for different LSTs; a far-field earthquakes, b near-field earthquakes with fling step effect, c near-field earthquakes with directivity effect

for all cases under consideration (i.e., for both square and rectangular LSTs) as shown in the sample plots drawn in Fig. 11.

### 4.4 Top Board Displacement

Figure 12 shows the mean percentage reduction in the TBDs (in X- and Y-directions) with the effective time period of the isolators. It is seen from the figures that the variation of the percentage reduction with the effective time period follows nearly the same trend as those observed for the shear forces and overturning moments. Further, the maximum percentage reduction of the TBDs in X- and Y-directions is of the order 75% except for the case of near-field earthquakes in which the maximum percentage reduction in X-direction TBD is about 80% occurring at  $T_b = 2.0$  s. As for the effect of the nature and PGA of the earthquake on the mean percentage reduction in TBDs, the same observations as those for shear forces and overturning moments hold.

Unlike the case of shear forces and overturning moments, the effect of the angle of incidence of the earthquake on

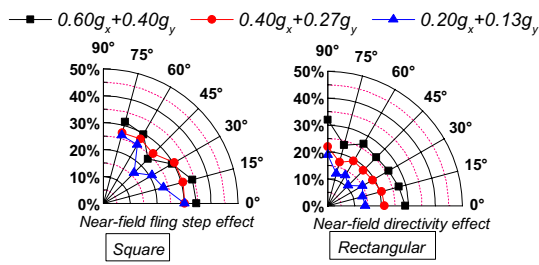
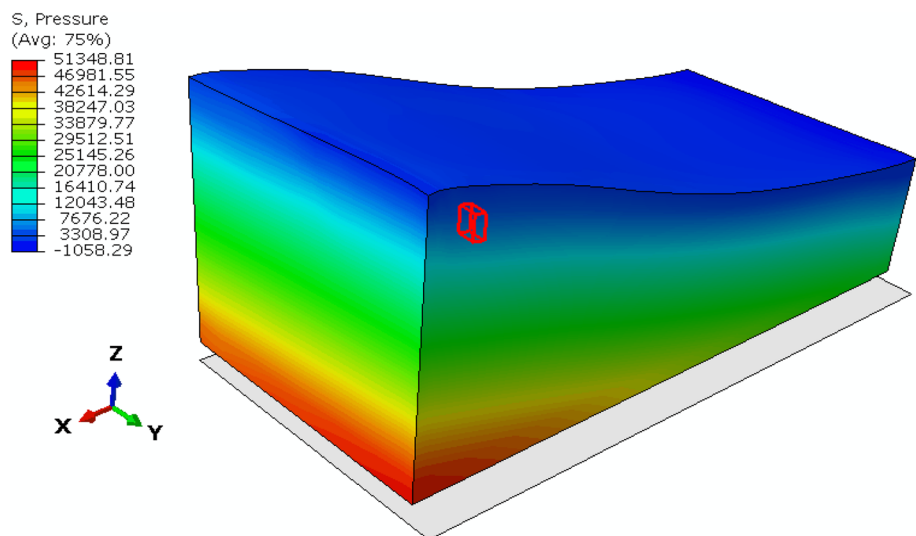


**Fig. 15** Variation of the percentage reduction in maximum hydrodynamic pressure with the angle of incidence for square and rectangular LSTs

TBDs is not insignificant, as shown in Fig. 13. For the square tank, the figures show that the maximum reduction in the TBD in the X-direction tends to occur at an angle of incidence of 15 degrees, nearly for all earthquakes. For the TBD in Y-direction, the far-field and near-field earthquakes with directivity effect show the maximum reduction in the TBD again at an angle of 15 degrees. For the near-field earthquakes with the fling step effect, the maximum reduction is observed at an angle of 60 degrees. For the rectangular tank, reduction in the TBD in the X-direction is decreased at an angle of incidence more significant than 60 degrees for the far-field earthquake and near-field earthquake with directivity effect. There is a mild increase in the reduction of responses at an angle of 45 degrees for the near-field earthquake with the fling step effect. As for the reduction in response in Y-direction, a decrease in responses is observed at an angle of incidence more significant than 45 degrees. Thus, the angle of incidence for a maximum decrease in TBD in the Y-direction depends upon the type of earthquake.

**Fig. 16** Hydrodynamic pressure contour in rectangular LST for Kocaeli earthquake (PGA = 0.6 g)



### 4.5 Hydrodynamic Pressure

The variation of the mean percentage reduction in the maximum hydrodynamic pressure at the base with the effective time period of the isolator is shown in Fig. 14. It is observed from the figure that the mean percentage reduction increases with the increase in the effective time period and reaches almost a stationary value at  $T_b = 2.5$  s. Further, it is seen that the nature of the variation differs with the type of the earthquake more as compared to the other response quantities.

The effect of the PGA on reducing the hydrodynamic pressure is also more pronounced than other response quantities. The impact of the angle of incidence of the earthquake on the decline of the hydrodynamic pressure is shown in Fig. 15. It is generally observed from the figure that the angle of incidence has a moderate effect on the response. There is a decrease in response reduction for the rectangular tank at the angle of incidence more significant than 60 degrees. Note that the nature of variation of the mean percentage reduction with the angle of incidence differs with the type of earthquake. Figure 16 displays the hydrodynamic pressure contour in the rectangular LST. It can be seen from the contour diagram that the magnitude of the pressure is higher under the crest of the sloshing wave.

### 4.6 Sloshing Height

Unlike other response quantities, the sloshing height is amplified in the base-isolated LSTs. The variation of the mean percentage amplification in the sloshing height with the effective time period for different types of earthquakes is shown in Fig. 17. It is seen from the figure that the amplification in sloshing height becomes almost stationary at  $T_b \geq 2.5$  s for both LSTs. For  $T_b$  less than 2.0 s, the variation of the percentage in amplification in sloshing height does not show any consistent pattern. It may increase or decrease

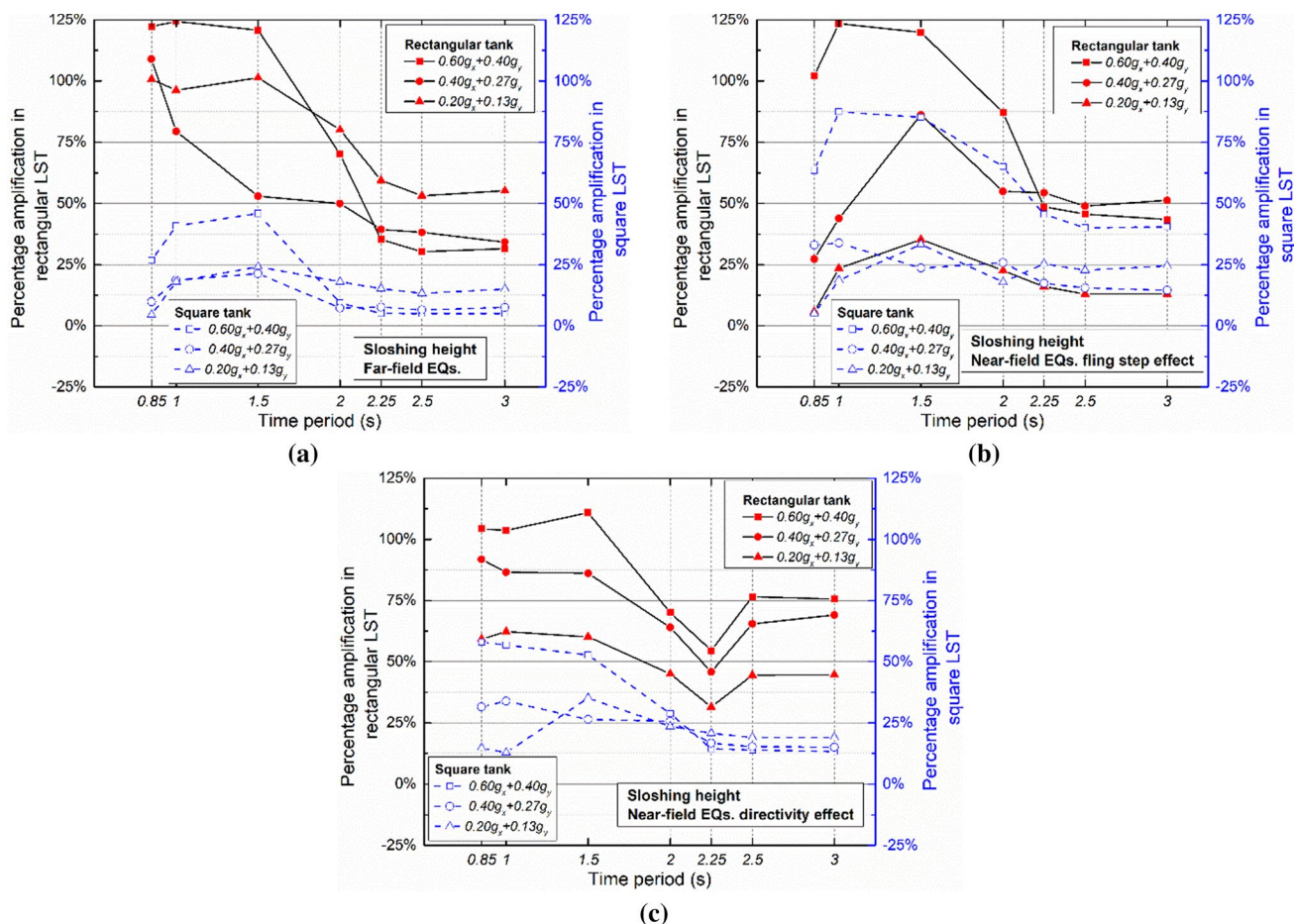


Fig. 17 Variation of the percentage amplification in sloshing height with the time period of the LRB isolators for different LSTs; **a** far-field earthquakes, **b** near-field earthquakes with fling step effect, **c** near-field earthquakes with directivity effect

depending upon the nature of the earthquake and PGA value. The maximum amplification of sloshing height can be as much as 50% for the square tank, and it occurs for the far-field earthquakes at a  $T_b = 1.5$  s. For the rectangular tank, at a smaller isolation period, the amplification in sloshing height could be more significant could be about 125%, denoting that the liquid will spill over the tank. However, beyond the isolation period of 2 s, the amplification in sloshing height is significantly reduced. Further, it can be seen from the figure that both the type and PGA values of the earthquake

have a considerable effect on the variation of amplification in sloshing height in square and rectangular LSTs.

The effect of the angle of incidence on sloshing amplification is shown in Fig. 18. It is seen from the figure that there is no significant effect of the angle of incidence on the amplification of sloshing height. The angle of incidence at which the maximum amplification takes place depends on the nature of the earthquake. The observation is valid for both square and rectangular tanks. Figure 19 shows the velocity contour of the sloshing height. It can be seen that from the figure that fluid particles closer to the LSTs surface follow the LST velocity profile. In contrast, the particles at the free surface are much freer and are developing turbulence at the free surface.

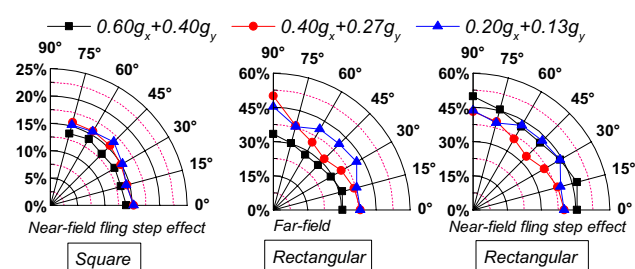


Fig. 18 Variation of the percentage amplification in the sloshing height with the angle of incidence for square and rectangular LSTs

### 4.7 Von-Mises Stress Distribution

The variation of the mean percentage reduction in the Von-Mises stress at the base with the effective time period of the isolator is shown in Fig. 20. It is observed from the figure that the mean percentage reduction



**Fig. 19** Velocity contour of the sloshing wave for rectangular LST for Landers earthquake (PGA = 0.6 g)

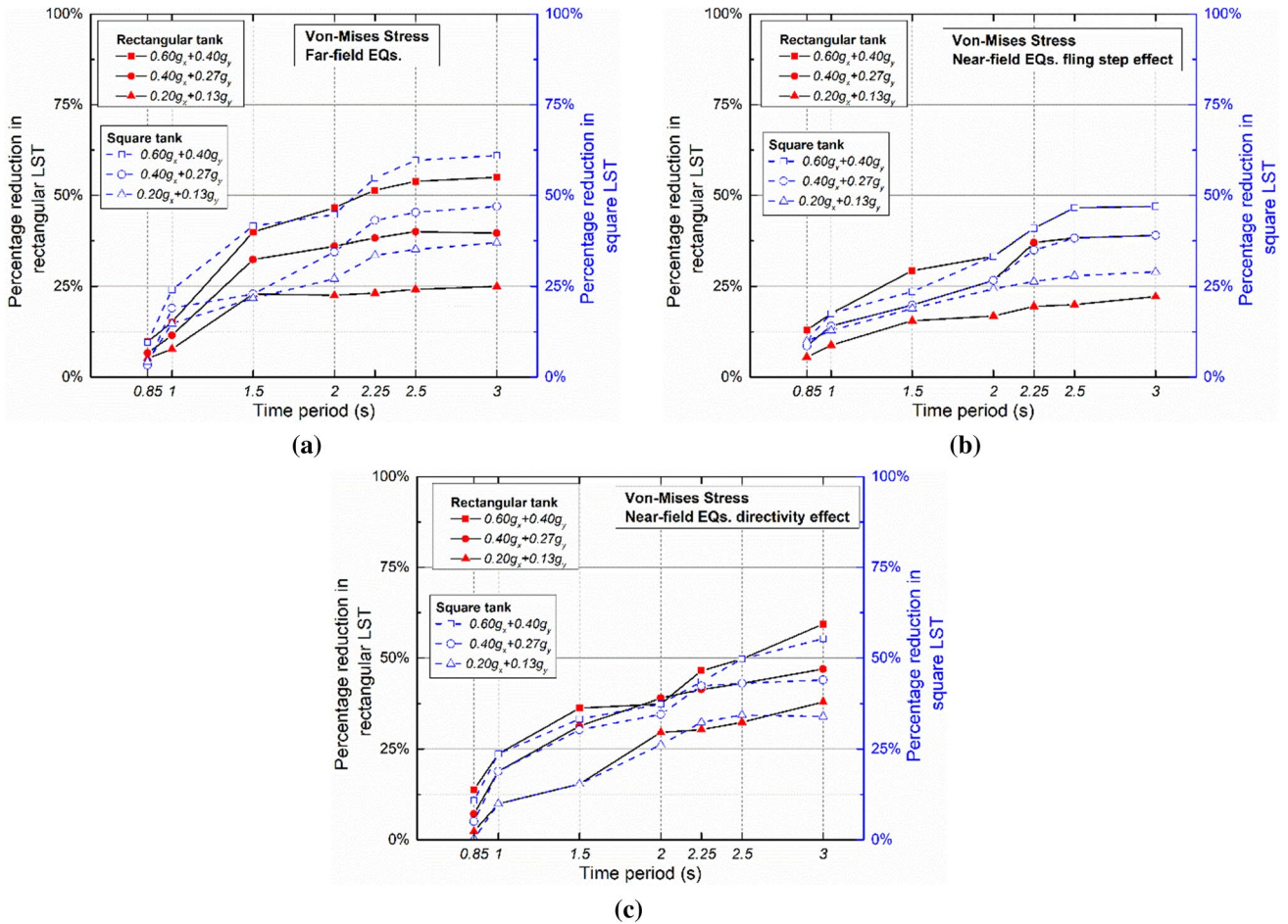
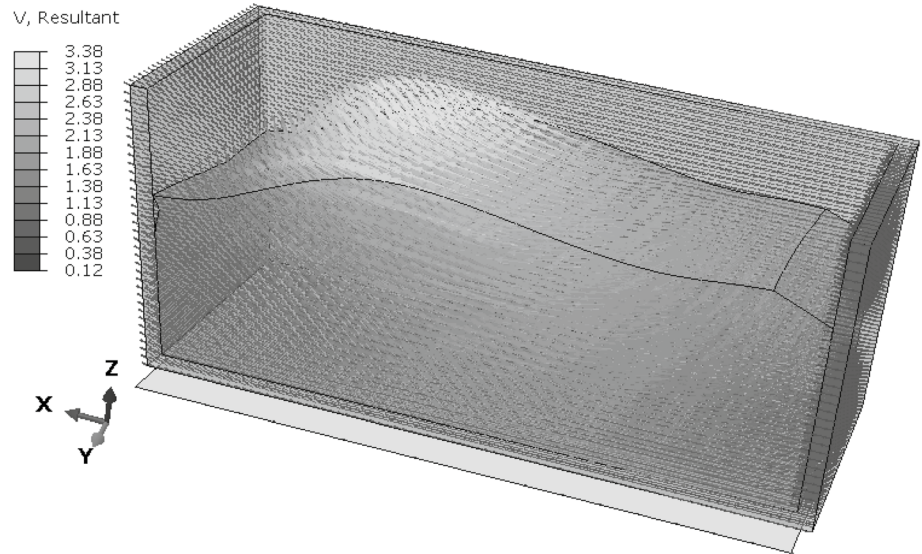


**Fig. 20** Variation of the percentage reduction in Von-Mises stress with respect to the time period of the LRB for **a** far-field earthquakes, **b** near-field earthquakes with fling step effect, **c** near-field earthquakes with directivity effect



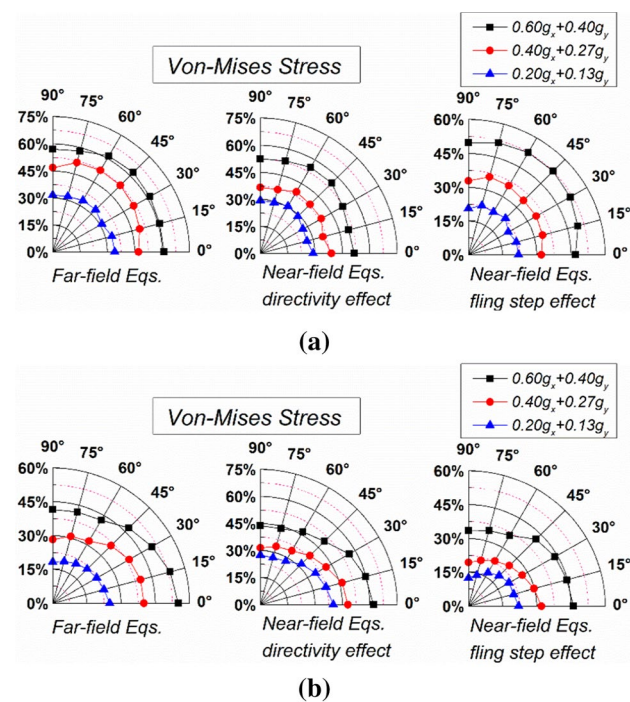
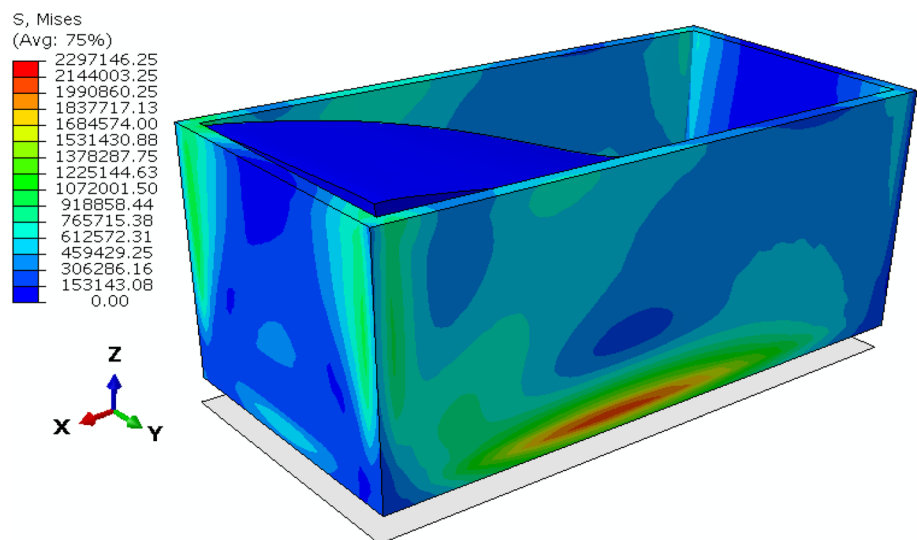


**Fig. 21** Variation of percentage reduction in Von-Mises stress with the angle of incidence for **a** square LST **b** rectangular LST

increases with the increase in the effective time period and reaches almost a stationary value at  $T_b = 2.5$  s for the square LST. In contrast, for the rectangular LST, the reduction in response becomes stable at  $T_b = 2.0$  s. It is seen that for the square LST, the maximum deduction is for the far-field earthquake, whereas for the rectangular LST, it is for the near-field earthquake with directivity effect.

Like the case of hydrodynamic pressure, the effect of PGA on reducing the Von-Mises stress is also very

**Fig. 22** Von-Mises stress contour for different earthquakes at PGA of 0.6 g for rectangular LST for Kocaeli earthquake



profound, especially for the case of far-field earthquakes in both LSTs. The impact of the angle of incidence of the earthquake on the reduction of the Von-Mises stress is shown in Fig. 21. It is generally observed from the figure that the angle of incidence has a moderate effect on the response. There is a slight increase in the reduction at an angle of 30–60 degrees for the square LST. However, for the rectangular LST increase in the decrease in response occurs at the angle of incidence of 0–45 degrees after that reduction becomes constant. Figure 22 shows the Von-Mises stress distribution for rectangular LSTs. It can be seen from the figures that the density of the stress contour is primarily focused at the base of the LSTs under the earthquakes; also, as the magnitude of the sloshing height becomes more prominent, the stress density gets amplified at the top corners of the walls.

#### 4.8 Optimum Effective Time Period of the Isolator

The above results indicate that the significant reduction in responses, except the sloshing height, occurs due to using the base isolation technique in the LSTs. To arrive at the optimum effective time period of the isolator, it is desired that the effective time period should be selected to achieve a comparatively high reduction in the response quantities of interest with less amplification in the sloshing height. For the present problem, considering the parametric study results, it is found out that  $T_b = 2.5$  s is the optimum effective time period for which the percentage reduction in responses is nearly 70–75% with a maximum sloshing amplification of the order of 25–30%. For the rectangular LST, the amplification in sloshing could be of the order of 50–70%, depending upon the type of earthquake.

## 5 Conclusion

An exhaustive parametric study investigates the effectiveness of the base isolation in the seismic protection of the 3D model LSTs. The base-isolated LSTs were simulated and analyzed in the ABAQUS platform under two-component earthquake excitations. The effect of base isolation on the response quantities of interest is studied by varying various factors. These include (i) the effective time period of the isolator, (ii) the nature of the ground motion, (iii) the PGA, and (iv) the earthquake incidence angle. The mean percentage change of response quantities of interest, namely the shear forces, overturning moments, TBDs, hydrodynamic pressure, sloshing height, and Von-Mises stress, is evaluated. Two concrete LSTs, one square and the other rectangular having  $H/L$  ratios of 0.6 and 0.3 with 5 LRB isolators, are taken as numerical examples.

The results of the numerical study lead to the following conclusions:

1. Reductions in the response quantities of interest and the amplification in sloshing height generally increase with the effective time period up to 2.5 s, after which they tend to become stationary.
2. The ratio of the optimum effective time period ( $T_b = 2.5$  s) to the impulsive and convective periods is 17 and 1.06 times, respectively; these ratios depend upon the problem at hand.
3. For the isolator with the optimum effective time period, the maximum reduction in the response quantities of interest is found to vary in the range of 70–75%; the maximum amplification of sloshing height varies between 25 and 30% for the square tank and 50%–70% for the rectangular tank depending upon the types of earthquake.
4. There is an optimum effective time period. A comparatively high reduction in response quantities can be achieved with less amplification of the sloshing height for the present problem; this effective time period is found to be about 2.5 s.
5. Both the earthquake and PGA nature affect the percentage reduction in response quantities of interest and the amplification in sloshing height.
6. The angle of incidence of the earthquake shows a slight to moderate effect on the reduction of different response quantities of interest and amplification in the sloshing height depending upon the type of earthquake.

**Authors' Contributions** All authors have equal contributions in the presented study.

**Funding** Not applicable.

**Data Availability** All data, models, and code generated or used during the study appear in the submitted article.

## Declarations

**Conflict of interest** The authors declare that they have no conflict of interest.

## References

1. Hosseinzadeh, N.; Kaypour Sangsari, M.; Tavakolian Ferdosiyeh, H.: Shake table study of annular baffles in steel storage tanks as sloshing dependent variable dampers. *J. Loss Prev. Process Ind.* **32**, 299–310 (2014). <https://doi.org/10.1016/j.jlp.2014.09.011>
2. Liu, W.K.: Finite element procedures for fluid–structure interactions and application to liquid storage tanks. *Nucl. Eng. Des.* **65**, 221–238 (1981). [https://doi.org/10.1016/0029-5493\(81\)90091-1](https://doi.org/10.1016/0029-5493(81)90091-1)
3. Crane, J.K.; Wilcox, R.B.; Hopps, N.W.; Browning, D.F.; Martinez, M.D.; Moran, B.D.; Penko, F.A.; Rothenberg, J.E.; Hensian, M.A.; Dane, C.B.; Hackel, L.A.: Integrated operations of the National Ignition Facility (NIF) optical pulse generation development system. In: *Third International Conference on Solid State Lasers for Application to Inertial Confinement Fusion*, p. 100 (1999)
4. Brunesi, E.; Nascimbene, R.; Pagani, M.; Beilic, D.: Seismic performance of storage steel tanks during the May 2012 Emilia, Italy, earthquakes. *J. Perform. Constr. Facil.* **29**, 1–9 (2012). [https://doi.org/10.1061/\(ASCE\)CF.1943-5509.0000628](https://doi.org/10.1061/(ASCE)CF.1943-5509.0000628)
5. Virella, J.C.; Godoy, L.A.; Su, L.E.; Suárez, L.E.: Dynamic buckling of anchored steel tanks subjected to horizontal earthquake excitation. *J. Constr. Steel Res.* **62**, 521–531 (2006). <https://doi.org/10.1016/j.jcsr.2005.10.001>
6. Kumbhar, O.; Kumar, R.; Panaiyappan, P.L.; Farsangi, E.N.: Direct displacement based design of reinforced concrete elevated water tanks frame staging. *Int. J. Eng.* **32**, 1395–1406 (2019). <https://doi.org/10.5829/ije.2019.32.10a.09>
7. Hosseini, M.; Goudarzi, M.A.; Soroor, A.: Reduction of seismic sloshing in floating roof liquid storage tanks by using a suspended annular baffle (SAB). *J. Fluids Struct.* **71**, 40–55 (2017). <https://doi.org/10.1016/j.jfluidstructs.2017.02.008>
8. Shekari, M.R.; Hekmatzadeh, A.A.; Amiri, S.M.: On the nonlinear dynamic analysis of base-isolated three-dimensional rectangular thin-walled steel tanks equipped with vertical baffle. *Thin-Walled Struct.* **138**, 79–94 (2019). <https://doi.org/10.1016/j.tws.2019.01.037>
9. Housner, G.W.: Dynamic pressures on accelerated fluid containers. *Bull. Seismol. Soc. Am.* **47**, 15–35 (1957)
10. Housner, G.W.: The dynamic behavior of water tanks. *Bull. Seismol. Soc. Am.* **53**, 381–387 (1963)
11. Vandiver, J.K.; Mitome, S.: Effect of liquid storage tanks on the dynamic response of offshore platforms. *Appl. Ocean Res.* **66**, 67–74 (1979)
12. Veletsos, A.S.: Seismic Effects in Flexible Liquid Storage Tanks (1974)
13. Warnitchai, P.; Pinkaew, T.: Modelling of liquid sloshing in rectangular tanks with flow-dampening devices. *Eng. Struct.* **20**, 593–600 (1998)
14. Wozniak, R.S.; Mitchell, W.: Basis of seismic design provisions for welded steel oil storage tanks. In: *Advances in Storage Tank Design*, American Petroleum Institute, Washington, USA (1978)
15. Faltinsen, O.M.; Rognebakke, O.F.; Lukovsky, I.A.; Timokha, A.N.: Multidimensional modal analysis of nonlinear sloshing in



- a rectangular tank with finite water depth. *J. Fluid Mech.* **407**, 201–234 (2000). <https://doi.org/10.1017/S0022112099007569>
16. Gavriljuk, I.P.; Lukovsky, I.A.; Timokha, A.N.: Linear and nonlinear sloshing in a circular conical tank. *Fluid Dyn. Res.* **37**, 399–429 (2005). <https://doi.org/10.1016/j.fluiddyn.2005.08.004>
  17. Virella, J.C.; Prato, C.A.; Godoy, L.A.: Linear and nonlinear 2D finite element analysis of sloshing modes and pressures in rectangular tanks subject to horizontal harmonic motions. *J. Sound Vib.* **312**, 442–460 (2008). <https://doi.org/10.1016/j.jsv.2007.07.088>
  18. Bakalis, K.; Fragiadakis, M.; Vamvatsikos, D.: Surrogate modeling for the seismic performance assessment of liquid storage tanks. *J. Struct. Eng.* **143**, 04016199 (2017). [https://doi.org/10.1061/\(ASCE\)ST.1943-541X.0001667](https://doi.org/10.1061/(ASCE)ST.1943-541X.0001667)
  19. Yazdaniyan, M.; Fu, F.: Parametric study on dynamic behavior of rectangular concrete storage tanks. *Coupled Syst. Mech.* **6**, 189–206 (2017). <https://doi.org/10.12989/csm.2017.6.2.18910.12989/csm.2017.6.2.189>
  20. Mandal, K.K.; Maity, D.: Nonlinear finite element analysis of water in rectangular tank. *Ocean Eng.* **121**, 595–601 (2016). <https://doi.org/10.1016/j.oceaneng.2016.05.048>
  21. Vern, S.; Shrimali, M.K.; Bharti, S.D.; Datta, T.K.: Attaining optimum passive control in liquid-storage tank by using multiple vertical baffles. *Pract. Period. Struct. Des. Constr.* **26**, 04021018 (2021). [https://doi.org/10.1061/\(asce\)sc.1943-5576.0000586](https://doi.org/10.1061/(asce)sc.1943-5576.0000586)
  22. Zhao, C.; Chen, J.; Wang, J.; Yu, N.; Xu, Q.: Seismic mitigation performance and optimization design of NPP water tank with internal ring baffles under earthquake loads. *Nucl. Eng. Des.* **318**, 182–201 (2017). <https://doi.org/10.1016/j.nucengdes.2017.04.023>
  23. Rawat, A.; Mittal, V.; Chakraborty, T.; Matsagar, V.: Earthquake induced sloshing and hydrodynamic pressures in rigid liquid storage tanks analyzed by coupled acoustic-structural and Euler–Lagrange methods. *Thin-Walled Struct.* **134**, 333–346 (2019). <https://doi.org/10.1016/j.tws.2018.10.016>
  24. Moslemi, M.; Farzin, A.; Kianoush, M.R.: Nonlinear sloshing response of liquid-filled rectangular concrete tanks under seismic excitation. *Eng. Struct.* **188**, 564–577 (2019). <https://doi.org/10.1016/j.engstruct.2019.03.037>
  25. Vern, S.; Shrimali, M.K.; Bharti, S.D.; Datta, T.K.: Behavior of liquid storage tank under multidirectional excitation. In: *Lecture Notes in Civil Engineering*, pp. 203–217. Springer (2021)
  26. Vern, S.; Shrimali, M.K.; Bharti, S.D.; Datta, T.K.: Impact of angle of incidence in rectangular liquid storage tanks. In: *Technologies for Sustainable Development*, pp. 68–72. CRC Press (2020)
  27. Vern, S.; Shrimali, M.K.; Bharti, S.D.; Datta, T.K.: Seismic behavior of baffled liquid storage tank under far-field and near-field earthquake. In: *Recent Advances in Computational Mechanics and Simulations*, pp. 445–456. Springer, Singapore (2021)
  28. Hosseini, M.; Farsangi, E.N.: Telescopic columns as a new base isolation system for vibration control of high-rise buildings. *Earthq. Struct.* **3**, 853–867 (2012). <https://doi.org/10.12989/eas.2012.3.6.853>
  29. Farsangi, E.N.; Tasnimi, A.A.; Yang, T.Y.; Takewaki, I.; Mohammadhasani, M.: Seismic performance of a resilient low-damage base isolation system under combined vertical and horizontal excitations. *Smart Struct. Syst.* **22**, 383–397 (2018)
  30. Wen, Y.: Method for random vibration of hysteretic systems. *J. Eng. Mech. Div.* **102**, 246–263 (1976)
  31. Lee, D.M.; Medland, I.C.: Base isolation systems for earthquake protection of multi-storey shear structures. *Earthq. Eng. Struct. Dyn.* **7**, 555–568 (1979). <https://doi.org/10.1002/eqe.4290070605>
  32. Bhandari, M.; Bharti, S.D.; Shrimali, M.K.; Datta, T.K.: The numerical study of base-isolated buildings under near-field and far-field earthquakes. *J. Earthq. Eng.* **22**, 989–1007 (2018). <https://doi.org/10.1080/13632469.2016.1269698>
  33. Panchal, V.R.; Jangid, R.S.: Behaviour of liquid storage tanks with VCFPS under near-fault ground motions. *Struct. Infrastruct. Eng.* **8**, 71–88 (2012). <https://doi.org/10.1080/15732470903300919>
  34. Rabiee, R.; Chae, Y.: Adaptive base isolation system to achieve structural resiliency under both short- and long-period earthquake ground motions. *J. Intell. Mater. Syst. Struct.* **30**, 16–31 (2019). <https://doi.org/10.1177/1045389X18806403>
  35. Jing, W.; Cheng, X.; Shi, W.: Dynamic responses of sliding isolation concrete rectangular liquid storage structure with limiting devices under bidirectional earthquake actions. *Arab. J. Sci. Eng.* **43**, 1911–1924 (2018). <https://doi.org/10.1007/s13369-017-2814-6>
  36. Hashemi, S.; Aghashiri, M.H.: Seismic responses of base-isolated flexible rectangular fluid containers under horizontal ground motion. *Soil Dyn. Earthq. Eng.* **100**, 159–168 (2017). <https://doi.org/10.1016/j.soildyn.2017.05.010>
  37. Rawat, A.; Matsagar, V.A.; Nagpal, A.K.: Numerical study of base-isolated cylindrical liquid storage tanks using coupled acoustic-structural approach. *Soil Dyn. Earthq. Eng.* **119**, 196–219 (2019). <https://doi.org/10.1016/j.soildyn.2019.01.005>
  38. Ozsarac, V.; Brunesi, E.; Nascimbene, R.: Earthquake-induced nonlinear sloshing response of above-ground steel tanks with damped or undamped floating roof. *Soil Dyn. Earthq. Eng.* **144**, 106673 (2021). <https://doi.org/10.1016/j.SOILDYN.2021.106673>
  39. Caprinuzzi, S.; Paolacci, F.; Bursi, O.S.; Dolšek, M.: Seismic performance of a floating roof in an unanchored broad storage tank: experimental tests and numerical simulations. *J. Fluids Struct.* **105**, 103341 (2021). <https://doi.org/10.1016/J.JFLUIDSTRUCTS.2021.103341>
  40. Bonet, J.L.; Miguel, P.F.; Fernandez, M.A.; Romero, M.L.: Analytical approach to failure surfaces in reinforced and biaxial bending. *J. Struct. Eng. Eng.* **130**, 1133–1144 (2006). [https://doi.org/10.1061/\(ASCE\)0733-9445\(2004\)130](https://doi.org/10.1061/(ASCE)0733-9445(2004)130)
  41. Ryan, K.L.; Kelly, J.M.; Chopra, A.K.: Nonlinear model for lead-rubber bearings including axial-load effects. *J. Eng. Mech.* **131**, 1270–1278 (2005). [https://doi.org/10.1061/\(ASCE\)0733-9399\(2005\)131:12\(1250\)](https://doi.org/10.1061/(ASCE)0733-9399(2005)131:12(1250))
  42. Sanaz, R.; Armen, D.K.: A stochastic ground motion model with separable temporal and spectral nonstationarities. *Earthq. Eng. Struct. Dyn.* **41**, 1549–1568 (2012). <https://doi.org/10.1002/eqe>
  43. Van Leer, B.: Towards the ultimate conservative difference scheme. IV. A new approach to numerical convection. *J. Comput. Phys.* **23**, 276–299 (1977). [https://doi.org/10.1016/0021-9991\(77\)90095-X](https://doi.org/10.1016/0021-9991(77)90095-X)
  44. Liyanapathirana, D.S.: Arbitrary Lagrangian Eulerian based finite element analysis of cone penetration in soft clay. *Comput. Geotech.* **36**, 851–860 (2009). <https://doi.org/10.1016/j.compgeo.2009.01.006>
  45. Dassault Systèmes Simulia Corp.: *Analysis User’s Manual Volume 1: Introduction, Spatial modeling, execution and output.* Abaqus 6.12. I, 831 (2012)
  46. Cheng, X.; Jing, W.; Gong, L.: Simplified model and energy dissipation characteristics of a rectangular liquid-storage structure controlled with sliding base isolation and displacement-limiting devices. *J. Perform. Constr. Facil.* **31**, 04017071 (2017). [https://doi.org/10.1061/\(ASCE\)CF.1943-5509.0001066](https://doi.org/10.1061/(ASCE)CF.1943-5509.0001066)
  47. Cheng, X.; Jing, W.; Gong, L.: Dynamic responses of a sliding base-isolated RLSS considering free surface liquid sloshing. *KSCE J. Civ. Eng.* **00**, 1–13 (2018). <https://doi.org/10.1007/s12205-018-0154-z>
  48. Jing, W.; Cheng, X.: Dynamic responses of sliding isolation concrete liquid storage tank under far-field long-period earthquake. *J. Appl. Fluid Mech.* **12**, 907–919 (2019). <https://doi.org/10.29252/JAFM.12.03.29180>



49. Ghallab, A.: Simulation of cracking in high concrete gravity dam using the extended finite elements by ABAQUS. *Am. J. Mech. Appl.* **8**, 7 (2020). <https://doi.org/10.11648/j.ajma.20200801.12>
50. Reyes, J.C.; Kalkan, E.: How many records should be used in an ASCE/SEI-7 ground motion scaling procedure? *Earthq. Spectra* **28**, 1223–1242 (2012). <https://doi.org/10.1193/1.4000066>
51. Goudarzi, M.A.; Danesh, P.N.: Numerical investigation of a vertically baffled rectangular tank under seismic excitation. *J. Fluids Struct.* **61**, 450–460 (2016). <https://doi.org/10.1016/j.jfluidstructs.2016.01.001>

